ORIGINAL PAPER

Mercapto grafted magnetic graphene oxide: synthesis, characterization, and application as a highly efficient and recoverable adsorbent for the mercury removal from contaminated waters

Maryam Karimi[1] · Mostafa Hassanisadi[2] · Tahereh Poursaberi[3]

Abstract

Heavy metals are present in sewage in several forms, increasing treatment problems and causing major environmental problems. Highly selective adsorption of the most dangerous heavy metals is one of the most important methods for water treatment and resource utilization. In this regard, a new mercapto grafted magnetic graphene oxide nanoadsorbent (MGO-SH) was synthesized and applied to remove excess mercury from aqueous solutions. To synthesize MGO-SH, GO was reacted with thionyl chloride ($SOCl_2$) and the acylated GO (GO-COCl) was grafted with p-Mercaptoaniline (MA). To characterize the synthesized nanoparticles, Fourier transform infrared spectroscopy (FT-IR), X-ray diffraction (XRD), transmission electron microscopy (TEM), X-ray photoelectron spectroscopy (XPS), and scanning electron microscope (SEM) were used. Some of the key parameters that might affect the removal efficacy, such as pH, nanoadsorbent amount, contact time, and some co-existing cations found in aqueous solutions, were also investigated. The optimum conditions to be as follows: adsorbent dosage 20 mg, pH of solution 6, and contact time of 20 min. The results showed that the equilibrium data for mercury sorption onto the proposed nanoadsorbent abide the Freundlich equation. Moreover, thermodynamic studies indicated that the adsorption is spontaneous and endothermic. Finally, the proposed nanoadsorbent was successfully used to remove mercury from the real water samples. Therefore, these nanosorbents could be good candidates for Hg (II) removal with the advantages of high sensitivity, high capacity, cost-effectiveness and ease of use.

Keywords Graphene oxide · Magnetic nanoparticle · Aqueous solution · Surface modification · Mercury ion

Introduction

Mercury, a persistent and extensively harmful pollutant that could accumulate in the food chain causes negative effects on the humans and ecosystem [1, 2]. Chlor-alkali, electroplating, dye, plastics, paper, dental filling materials, batteries, pesticides, herbicides, and insecticides are some of the industrial sources that produce Hg (II) polluted wastewaters [3–6]. Mercury exists in three oxidation states including elemental mercury (Hg^0), methylmercury (Hg (I)), and inorganic mercury (Hg (II)) in biological and environmental systems [2]. According to the standards, 2 and 10 μg L^{-1} are the permitted levels of mercury for drinking water and surface water discharge, respectively [6]. It is therefore crucial to develop efficient methods of mercury removal from water resources.

Several methods have been proposed to treat mercury containing wastewaters. These include membrane separation, chemical precipitation, ion exchange, and adsorption [7–10]. Amongst these methods, adsorption is the most studied one because it offers many advantages in terms of process design, operation, and cost [11–18]. To treat Hg (II)–contaminated wastewaters, various adsorbents such as activated carbons, zeolites, polymers, and biomass materials [19–21] have been extensively developed. However, the majority of these materials are unsuitable due to poor

✉ Maryam Karimi
  m.karimi81@gmail.com

  Mostafa Hassanisadi
  mhsaadi@ripi.ir

1 Physics and Accelerators Research School, Nuclear Science and Technology Research Institute (NSTRI), Tehran, Iran

2 Nanotechnology Research Center, Research Institute of Petroleum Industry, Tehran, Iran

3 Department of Instrumental Analyses, Research Institute of Petroleum Industry, Tehran, Iran

selectivity, weak regeneration, and difficulty in separating the adsorbed compound from the mother solution [22].

Due to its wide surface area, porous structure, flexibility, and chemical stability, graphene has attracted great attention. It is a great candidate for the generation of graphene-based composite materials [23–25]. On the other hand, magnetite nanoparticles (Fe_3O_4 NPs) with their small size and high surface energy have a superparamagnetic property that allows them to be recycled by magnetic separation and could easily be regenerated [26, 27]. A combination of the high adsorption capacity of graphene and the magnetic properties of the Fe_3O_4 NPs could provide both of these benefits in a single nanoadsorbent.

Surface modification of the GO could induce selective targeting. Reports show that Hg (II) has a high affinity towards sulfur-containing ligands and they have been successfully applied for mercury selective electrode construction [28, 29]. Therefore, immobilization of S-containing ligands on the surface of GO-based magnetic nanoparticles produces a good adsorbent for selective mercury removal.

In this paper, magnetic graphene oxide (MGO) nanoadsorbent functionalized with p-mercaptoaniline was fabricated and characterized by various methods. Furthermore, the potential of MGO-SH hybrids as an effective adsorbent for mercury abatement from aqueous media is demonstrated. The thermodynamic and kinetic information of the adsorption process were studied to shed some light on the process of the adsorption of mercury molecules onto the proposed nanoadsorbent.

Materials and methods

Materials

p-mercaptoaniline (C_6H_7NS), nature flake graphite, ferrous chloride tetrahydrate ($FeCl_2.4H_2O$), ferric chloride hexahydrate ($FeCl_3.6H_2O$), ammonia solution 25%, sodium hydroxide (NaOH), hydrochloric acid (HCl, 36.5%), sulfuric acid (H_2SO_4, 98%), potassium permanganate ($KMnO_4$), sodium nitrate ($NaNO_3$), hydrogen peroxide (H_2O_2, 30%), thionyl chloride ($SOCl_2$), tetrahydrofuran (THF), N,N-dimethylformamide (DMF), ethanol (C_2H_5OH), thiourea, diethyl ether ($C_2H_5)_2O$ and triethylamine (Et_3N) were all purchased in analytical grade from Merck (Darmstadt, Germany). A standard solution of Hg (II) (1000 mg L^{-1}, in HNO_3 2 mol L^{-1}) was purchased from Merck (Darmstadt, Germany). The standard stock solutions for other metal ions were purchased from Sigma-Aldrich. The stock solutions were stored at 4 °C in the dark. The working standards were obtained by weekly diluting with water. Triply distilled deionized water was used throughout.

Preparation of GO-SH

Hummer's method was used for the preparation of GO. In a typical experiment [30], graphene oxide (GO) (30 mg) was refluxed in $SOCl_2$ (20 mL) in the presence of DMF (0.5 mL) at 70 °C under argon atmosphere for 24 h. At the end of the reaction, excess $SOCl_2$ and solvent were removed by distillation. The acylated graphene oxide (GO-COCl) was washed with anhydrous THF and vacuum dried. In the presence of triethylamine (Et_3N, 0.5 mL), GO-COCl was allowed to react with paramercaptoaniline (30 mg) in anhydrous DMF (10 mL) at 130 °C for 72 h under argon. The solution was cooled to room temperature and then poured into ether (300 mL) to precipitate the product. The precipitate was isolated by using centrifugation. The excess p-mercaptoaniline and other impurities were removed through washing cycles, which included sonication, filtration, and re-suspension of the solid in THF five times. Following the above procedure, the precipitate (GO-SH) was washed with ethanol and ether and then washed with a small quantity of water to remove triethylamine and finally dried under vacuum.

Magnetization of GO-SH

The MGO-SH nanoadsorbent was synthesized by coprecipitation of $FeCl_3.6H_2O$ and $FeCl_2.4H_2O$, in the presence of GO-SH. An aqueous solution of iron salts containing iron (II) chloride and iron (III) chloride was prepared in a 1:2 mol ratio. 100 mg of GO-SH in 40 mL of water was ultrasonicated for 30 min; 50 mL of $FeCl_3.6H_2O$ (500 mg) and $FeCl_2.4H_2O$ (190 mg) dissolved in DI water was added, and the solution was stirred at room temperature under N_2 atmosphere. The temperature was raised to 85 °C and a 25% ammonia solution was added increasing the pH to 10. After stirring the solution at high speed for 45 min, it was cooled to room temperature. The precipitate was isolated by a strong magnet and the impurities were removed by washing with DI water. The MGO-SH nanoadsorbent was washed with absolute ethanol and dried under vacuum at 60 °C. The preparation process of MGO-SH is schematically shown in Fig. 1.

Sample characterization

The XRD pattern of the MGO-SH nanoadsorbent was obtained using a PW-1840 diffractometer (Philips Co.) with Cu-Kα radiation ($\lambda = 1.54178$ A°) in the 2θ range of 5–80°. XPS spectra were recorded by 8025-BesTec twin anode XR3E2 x-ray source system. Transmission electron microscopy was performed using a Zeiss 900 TEM at a voltage of 80 kV and scanning electron microscope (SEM, MIRAII LMU TESCAN) were used to determine the morphology
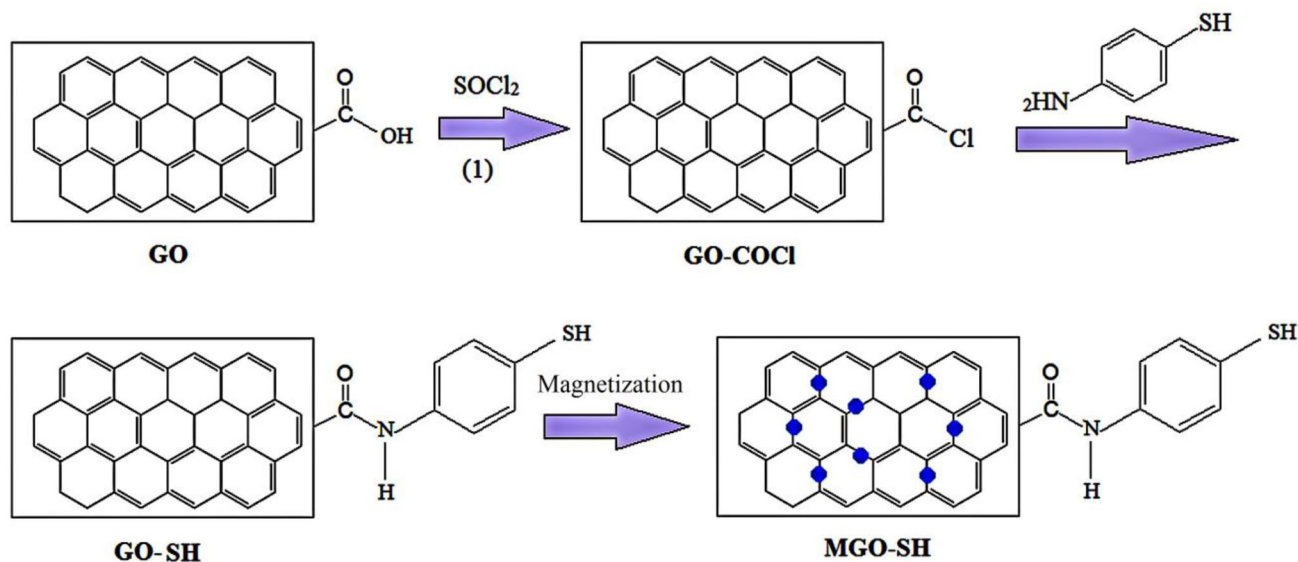
Fig. 1 The preparation process of MGO-SH

of the nanoadsorbent. Vertex70 FT-IR spectrophotometer (Bruker Co.) was used for recording the FT-IR spectra. All absorption measurements were performed with Perkin-Elmer Zeeman 3030 atomic absorption spectrometer equipped with the HGA 600 atomizer. The pH adjustment was carried out by a Metrohm 691 pH meter (Switzerland).

Batch adsorption experiments

In batch experiments, 50 mL aqueous solution of Hg (II) (10 mg L^{-1}) and 20 mg of the nanosorbent were added to a stoppered flask, and at 200 rpm were shaken for 20 min at room temperature. The adsorbent was separated magnetically, and then the concentration of the residual Hg (II) was determined by an atomic absorption spectrometer. The removal efficiency was calculated using Eq. (1):

$$\text{Mercury removal efficiency (\%)} = \left[\frac{C_0 - C_r}{C_0} \right] \times 100 \quad (1)$$

where C_0 and C_r are the initial and final concentrations of the mercury ion, respectively.

Adsorption isotherms

To comprehend the adsorption process, it is essential to have some information about the adsorption isotherms of the adsorbent [31]. To obtain the mercury adsorption isotherms onto the MGO-SH surface, various quantities (10–50 mg) of MGO-SH were added to the vials containing 50 mL of 10 mg L^{-1} Hg (II) solution. The solutions were stirred for 20 min to achieve equilibrium. After the

separation of nanoparticles, the Hg (II) residual was measured in an aqueous solution. Based on the mass balance equation, the amount of the adsorbed Hg (II) onto MGO-SH was calculated:

$$q_e = \frac{V(C_0 - C_e)}{m} \quad (2)$$

where q_e (mg g^{-1}) is the adsorption capacity, V is the volume of the Hg (II) solution (L), C_0 and C_e are the initial and equilibrium Hg (II) concentrations (mg L^{-1}), and m is the mass (g) of the dry MGO-SH added.

Several isotherm models are proposed for the equilibrium adsorption [32–36], but the most popular ones are Longmuir and Freundlich. The Langmuir hypothesis is predicated on the idea that sorption occurs at particular homogeneous sites within the adsorbent. It is then presumed that if a molecule has occupied a region, no further adsorption will occur there. As a result, a saturation value is reached above which no further sorption will occur theoretically. Assuming monolayer adsorption occurring on a homogeneous adsorbent surface, the linearized form of the Longmuir isotherm is expressed as:

$$\frac{C_e}{q_e} = \frac{1}{bq_{max}} + \frac{C_e}{q_{max}} \quad (3)$$

where C_e is the equilibrium concentration of Hg (II) remaining in the solution (mg L^{-1}). q_e is the quantity of adsorbate adsorbed per unit mass of adsorbent at equilibrium (mg g^{-1}). The Langmuir constants q_{max} and b are calculated by taking the slope and intercept of the line and plotting (C_e/q_e) versus C_e.

The Freundlich isotherm is derived by assuming a heterogeneous surface with a non-uniform distribution of heat of adsorption over the surface. The linearized form of the Freundlich equation is expressed as follows:

$$\log q_e = \log K_F + \frac{1}{n} \log C_e \qquad (4)$$

where K_F is Freundlich constant and 1/n is the heterogeneity factor. K_F represents the capacity of the adsorbent for the adsorbate, n is the reaction order, while 1/n is a function of the strength of adsorption.

Results and discussion

Characterizations

X-ray diffraction measurements were carried out to investigate the material phase structure as shown in Fig. 2. The peak observed at $2\theta = 10.2°$, which corresponds to (0 0 1) crystal planes of GO, was attributed to the diffraction of graphene [37] and indicated that the graphene structure was preserved after functionalization. All of the other significant diffraction peaks at $2\theta = 30.0°$, 35.3°, 42.9°, 53.4°, 56.9° and 62.5° of the MGO-SH sample matched well with the JCPDS card (19–0629) which are assigned to (220), (311), (400), (422), (511), and (440) of the crystal planes of Fe_3O_4, respectively.

The images of the prepared nanoadsorbent were obtained by SEM and TEM. As shown in Fig. 3, the iron oxide nanoparticles were successfully coated on the surface of GO to form MGO nanoadsorbent.

To investigate the interaction between p-mercaptoaniline and GO, the FT-IR spectrum was recorded (Fig. 4). It was observed that the GO sheets carried adsorbed water molecules and structural OH groups (a strong absorption band at 3410 cm^{-1} due to O–H stretching vibrations). C=O (the C=O stretching vibrations from carbonyl and carboxylic groups at 1734 cm^{-1}), and C–O (C–OH stretching vibrations at 1200 cm^{-1} or O–C–O stretching vibrations at 1050 cm^{-1}) groups, indicated the attachment of oxo-groups on GO sheets after the chemical oxidation of the flake graphite. The

spectra also showed a band around 1520 cm^{-1} corresponding to the C=C stretching vibrations of carbon–carbon bonds in the aromatic ring. The band at 1689 cm^{-1} corresponds to the C=O characteristic stretching band of the amide group; the stretching band of the amide C–N peak appeared at 1260 cm^{-1}. These results proved that the p-mercaptoaniline is covalently attached to the carboxylic groups of GO through the formation of a stable amide bond. The spectra also showed S–H stretching vibration of the mercapto group at 2540 cm^{-1} and the weak band at 560 cm^{-1} was assigned to the C–S stretching vibrations. The peak at 584 cm^{-1} was the characteristic peak of Fe_3O_4.

X-ray photoelectron spectroscopy (XPS) was used to determine the chemical composition of the GOM-SH composite. Figure 5a illustrates the C1s deconvolution spectrum of GOM-SH, and six different carbon-containing functional groups of (a) the non-oxygenated carbon (–C=C SP^2) at 283.5 eV, (b) the non-oxygenated carbon (–C=C SP^3) at 285.0 eV, (c) the carbon (C–N) at 285.3 eV, (d) the hydroxyl carbon (C–OH) at 286.0 eV, (e) the carbonyl (C=O) at 287.4 eV, (f) the carboxylate carbon (O–C=O) at 289.5 eV were observed. Five peaks are present in the O1s spectrum of GOM-SH (Fig. 5b), which correspond to Fe–O at 530.7, N–C=O at 532.0, C(O) OH at 532.7 eV, C–OH at 533.8 eV, and H$_2$O at 535.3 eV. The peak at 530.7 eV is the contribution of the anionic oxygen in Fe_3O_4. The formation of Fe_3O_4 nanoparticles was also confirmed by the high-resolution Fe 2p spectrum (Fig. 5c), in which the peaks at 725.2 and 711.6 eV are characteristic of Fe 2p1/2 and Fe 2p3/2 of Fe_3O_4. In addition, the presence of C1s peak at 285.3 eV (C–N) which corresponds to the amide group confirmed the covalent bond formation between p-mercaptoaniline (MA) and GO-COCl [38]. Also, O1s peak at ~ 532.0 eV (N–C=O) proved that MA was grafted to the surface of graphene oxide by amide bonding.

Adsorption experiments

Effect of solution pH

The solubility and the form in which a metal is present in the solution and the ionization of functional groups on
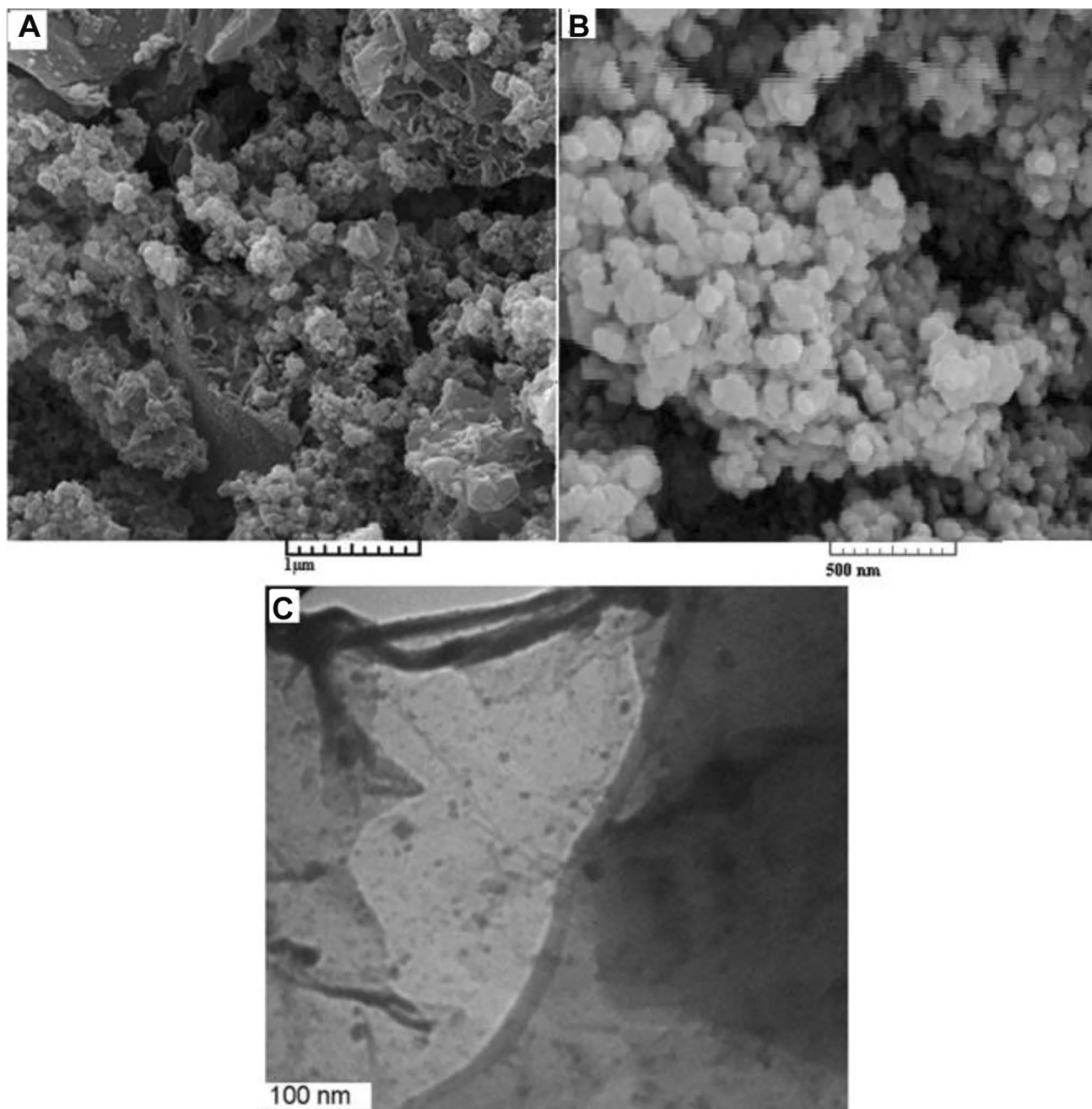
**Fig. 2** X-ray diffraction pattern of MGO-SH
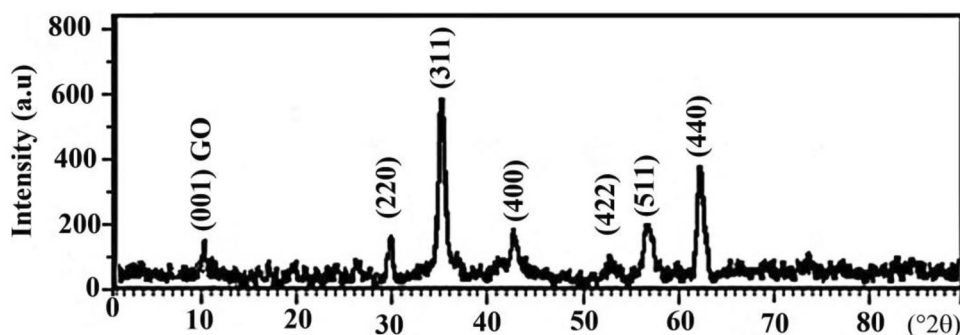
Fig. 3 SEM images **a** low-magnification, **b** high-magnification and TEM image **c** of MGO-SH

the surface of the adsorbent are affected by the pH of the solution [39, 40]. The performance of the nanoadsorbent was studied in the pH range of 2.0–7.0 (Fig. 6). The sorption of mercury initially increased with pH and a plateau occurred at pH 4 onwards. The surface chemistry in an aqueous phase could explain this pH-dependent trend. Hg (II) is classified as a soft metal ion according to Pearson's hard-soft acid–base theory (HSAB) [41] and selectively interacts with nitrogen and sulfur atoms of the molecules [42, 43].

It is proved that surface charge is a key factor for the adsorption of metal ions [44, 45] and it is very much dependent on the pH of the solution. The surfaces of modified nanoparticles are covered with mercapto groups. At low pH, adsorption sites are passivated as the mercapto groups are protonated, and hence mercury adsorption is suppressed. The adsorption studies at more alkaline solutions (pH > 7) were not carried out; because mercuric ions might precipitate. Therefore, PH 6 was selected as the optimum pH throughout the experiments.

Fig. 4 FT-IR spectrum of MGO-SH
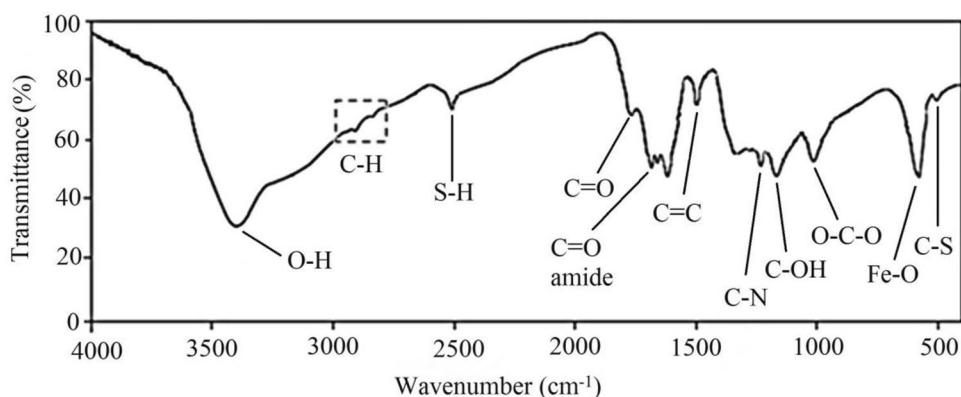
Effect of adsorbent dosage

The optimum amount of the nanoadsorbent which can remove mercury ions from aqueous solution was found by batch-mode sorption. In due course, various amounts (10–50 mg) of MGO-SH nanoadsorbent were examined and the mercury removal efficiency as a function of nanoadsorbents dosage was monitored. It is shown that increases in nanoadsorbent dosage increase the mercury removal percentage; with stirring time 20 min, removal percentage reached steady state after addition of 20 mg of MGO-SH nanoadsorbents to 50 mL aqueous solution containing 10 mg L^{-1} mercury ion pH 6. For subsequent experiments, 20 mg was selected as the optimum amount of the nanoadsorbent.

Effect of contact time

The time dependence of mercury removal was evaluated in the range of 10–90 min. To perform this experiment, 10 mg of nanoadsorbent was added to 50 mL of mercury solution at a concentration of 10 mg L^{-1} at pH 6, and then it was stirred at laboratory temperature at 200 rpm. The results showed that the adsorption of mercury ion on the nanoadsorbent is achieved in the first 20 min and then remained constant afterward. Therefore, 20 min was chosen as the optimal time for further experiments.

Effect of initial concentration

To investigate the relationship between the initial concentration of Hg (II), q_e and the adsorption percentage of Hg (II) on the MGO-SH, different concentrations of Hg (II) in the range of 10 mg L^{-1} to 700 mg L^{-1} were tested (Fig. 7). The experimental results showed that the equilibrium sorption capacity of the adsorbent increases with increasing the initial concentration of Hg (II) ion. This is since the higher the initial concentration of Hg (II) ions, the greater the driving forces of the concentration gradient at the solid–liquid interface which leads to an increase of the adsorption of

Hg (II) ions. When the initial concentration of Hg (II) ions increases from 10.0 to 500.0 mg L^{-1}, the equilibrium amount of the adsorbed Hg (II) ions (q_e) increases from 24.6 to 550.0 mg g^{-1} and the mercury removal efficiency decreases from 98.5 to 44.0%. This decrease is likely related to the reduction of the available sites on the adsorbent because of the occupation of these sites with mercury at higher concentrations of Hg (II) ions. When there are more Hg (II) ions in the solution, most of the active sites are involved in the adsorption process and the adsorption capacity reaches a steady level, indicating saturation of the available binding sites on the adsorbent. It should be noted that at lower initial concentrations (below 10 ppm), a 98.5% removal can be achieved by MGO-SH adsorbent, that is, for these mercury concentrations, the adsorbent is effective for complete mercury removal [46–48].

Adsorption thermodynamics

To investigate the effect of temperature on the adsorption process of mercury onto MGO-SH, the removal efficiency of a 10 mg L^{-1} mercury solution under optimal conditions (i.e., contact time: 20 min, pH 6.0 and adsorbent dosage: 20 mg) was monitored in the temperature range of 278–308 K (Fig. 8). The figure shows the temperature dependency of the efficiency and the endothermic nature of the adsorption process.

According to van't Hoff equation, the slope and intercept of the plot $\ln(q_e/C_e)$ versus $1/T$ determine the changes of enthalpy (ΔH) and entropy (ΔS), respectively:

$$\ln\left(\frac{q_e}{C_e}\right) = \frac{\Delta S}{R} - \frac{\Delta H}{RT} \tag{5}$$

where R is the universal gas constant (8.314 J mol^{-1} K) and T is the absolute temperature (K). Thermodynamic parameters of adsorption of mercury onto the nanoadsorbent are shown in Table 1.
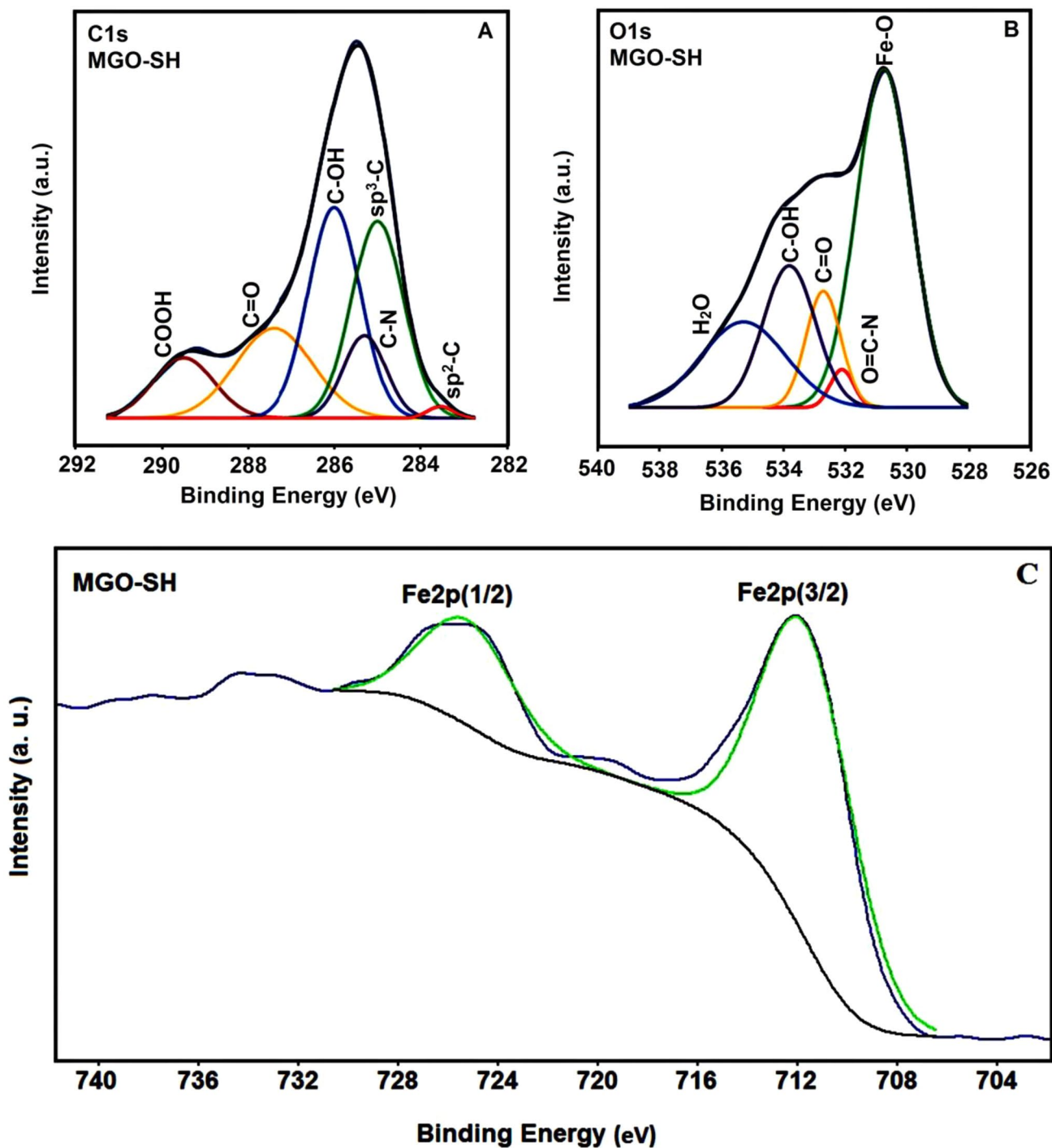
Fig. 5 XPS spectra of MGO-SH **a** C1s, **b** O1s, **c** Fe 2p

The feasibility and the spontaneity of the adsorption process could be concluded from the negative free energy of the adsorption processes (ΔG) at all temperatures. The increase in ΔG values with an increase in temperature shows an increase in the feasibility of sorption at higher temperatures. The endothermic nature of the process could be deduced from the positive value of ΔH. In other words, mercury diffusion into the adsorbent surface is an endothermic process. The positive value of ΔS shows that an increase in randomness occurs at the interface during the sorption process. It is notable that the adsorption process with ΔG values between -20 and 0 kJ mol^{-1} corresponds
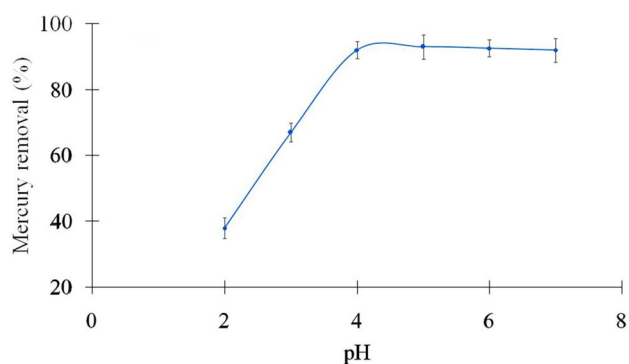
Fig. 6 The pH influence on the removal efficiency of Hg (II). Experimental conditions: MGO-SH dosage 10 mg, stirring time 20 min, Hg (II) volume 50 mL, initial Hg (II) concentration 10 mg L^{-1}
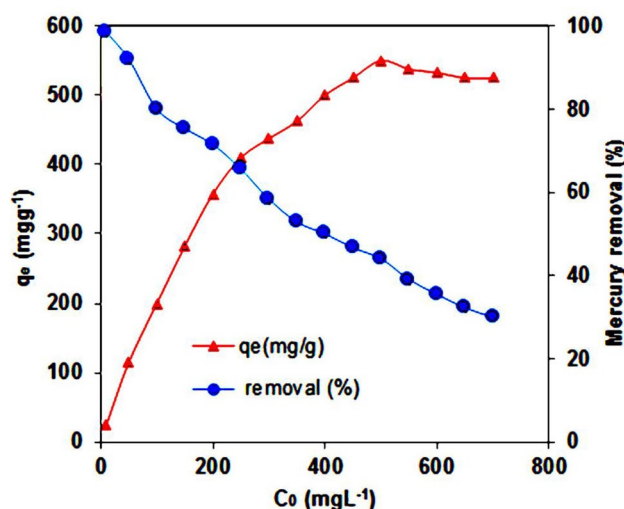

Fig. 7 The relationship between the initial concentration of Hg (II) and the equilibrium adsorption (q_e) (▲) and the adsorption percentage (●)
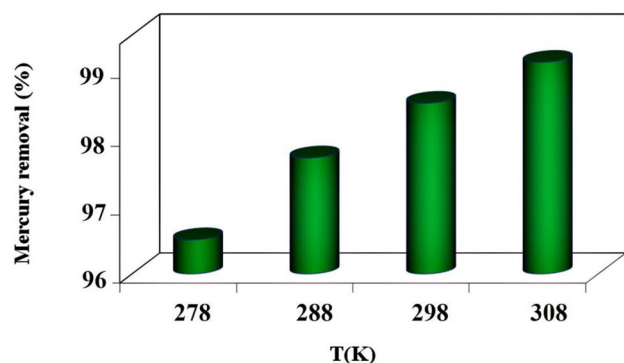

Fig. 8 Effect of temperature on the removal of mercury. Experimental conditions: pH 6.0, stirring time 20 min, initial Hg (II) concentration 10 mg L^{-1} and nanoadsorbent dosage 20 mg

to spontaneous physical process—physisorption—while values between -80 and -400 kJ mol^{-1} correspond to chemisorption processes [49–51]. The ΔG values obtained in this study lead to the conclusion that the adsorption process is dominated by physisorption. This also is supported by the fact that $\Delta H < 40$ kJ mol^{-1}, indicating a physical adsorption process [49–51].

Adsorption isotherm modeling

Longmuir and Freundlich models were used for the equilibrium adsorption data analysis of mercury on MGO-SH. The fitted experimental data with both models are shown in Fig. 9. Table 2 summarizes the models constants and correlation coefficients (R^2). Adsorption of the mercury on MGO-SH is better described by Freundlich model with the greater R^2. The value of $1/n$ (0.43), which is less than 1, indicated the heterogeneity of the MGO-SH with an exponential energy distribution of surface active-sites [52]. The Freundlich constant ($1/n$) is related to the adsorption intensity of the adsorbent. When $0.1 < 1/n \leq 0.5$, adsorption occurs readily; when $0.5 < 1/n \leq 1$, there is a difficulty with the absorption and when $1/n > 1$, adsorption is quite difficult [53]. The $1/n$ and K_F values of adsorption of Hg (II) on the MGO-SH were 0.43 and 64.56, respectively, indicating that the mercury could easily be adsorbed on the MGO-SH nanoadsorbent with a high adsorption capacity [54, 55].

Removal of mercury from real samples

In order to evaluate the reliability of the method, several real water samples were analyzed by cold vapor atomic absorption spectrometry (CVAAS). The batch adsorption experiment was carried out on 50 mL of these samples under optimal conditions, i.e., contact time: 20 min, pH 6.0, and adsorbent dosage: 20 mg. The data obtained with the proposed methods for spiked and real samples are presented in Table 3. The removal efficiency ranged from 94.9 to 98.5% indicating a remarkable ability of the synthetic adsorbent for Hg (II) removal from real samples. Moreover, the precisions of the applied method were assessed by calculation of the relative standard deviation (RSD %) based on three cumulative replicates for each elimination assay. It can be seen from Table 3 that the RSDs% are as low as 2.3%, indicating that the precision of the applied method is acceptable.

Selectivity test

Toxic metallic species rarely exist individually in wastewaters, and other metal ions are also present. Therefore, mercury removal from real samples is dependent upon the presence of other cations which could compete for the binding sites with mercury and cause lower mercury uptake. The

Table 1 Thermodynamic parameters of mercury adsorption onto the MGO-SH nanoadsorbents

ΔS_0 (J mol^{-1} K^{-1})	ΔH_0 (kJ mol^{-1})	ΔG_0 (kJ mol^{-1})			
		278 K	288 K	298 K	308 K
151.89	32.54	− 9.69	− 11.21	− 12.72	− 14.24
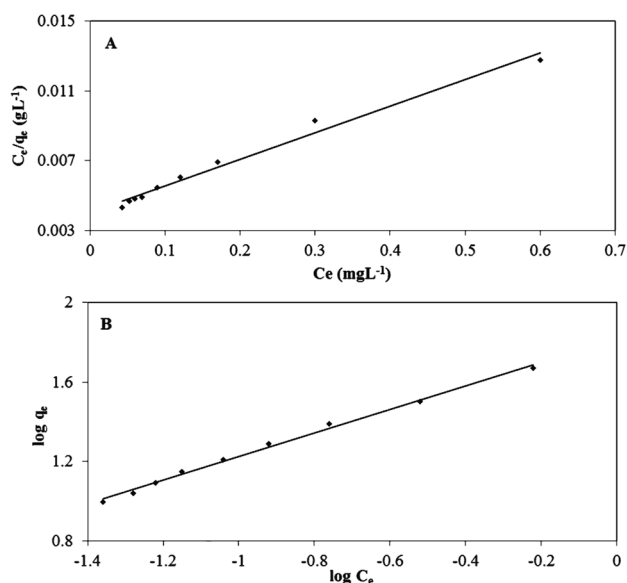
Fig. 9 Isotherm plots of Hg (II) adsorption onto MGO-SH: **a** Langmuir isotherm and **b** Freundlich isotherm

Table 2 Adsorption isotherms parameters of Hg^{2+} onto the MGO-SH nanoparticles

Langmuir model			Freundlich model		
q_{max}	b	R^2	Log K_F	$1/n$	R^2
66.66	3.65	0.984	1.81	0.43	0.995

Table 3 Removal of Hg^{2+} from different water samples using MGO-SH

Water samples	Hg^{2+} Conc. (mg L^{-1}) Mean ± S.D.[a]	Added Hg^{2+}	Removal % (RSD%)[b]
Deionized water	n.d.[c]	10	98.5 (2.4)
Tap water[d]	n.d	10	98.0 (2.6)
Wastewater[e]	9.8 ± 0.3	0	97.1 (2.9)
	9.8 ± 0.3	10	94.9 (2.7)

Optimal conditions: contact time: 20 min, pH 6.0 and adsorbent dosage: 20 mg

[a]Standard deviation ($n = 3$)

[b]Relative standard deviation

[c]Not detected

[d]The tap water was taken from a laboratory of Research Institute of Petroleum Industry (Tehran, capital of Iran)

[e]The wastewater was taken from heavy metal laboratory of Research Institute of Petroleum Industry

optimal experimental conditions described above were used to study whether or not other cations could act as interfering ions during the mercury removal (Fig. 10). These experiments were performed with a fixed mercury concentration of 10 mg L^{-1}, while the concentration of each coexisting cations varied within two orders of magnitude. The amount of the foreign ion causing a change of ± 5% in the mercury removal efficiency was defined as the tolerance limit. In the presence of the ten folded concentrations of copper, nickel, and cadmium, fifty folded of lead, and one hundred folded of sodium and calcium ions, the removal percentage of mercury remained within the tolerance limit (Fig. 10). Consequently, the aforementioned cations had no significant effect on the Hg (II) removal by MGO-SH nanoadsorbent; this fact could be assigned to the selective interaction of mercapto group with mercury ions.

Recovery of mercury ion and reusability of MGO-SH

According to the literature [56, 57], in the absence of thiourea, Hg (II) adsorbed on SH groups cannot be quantitatively eluted. Hence, a mixed solution of HCl and thiourea was used for fast and quantitative elution of mercury from the adsorbent. Eluents of HCl at concentrations from 0.1 to 3.0 M mixed with 2% (m/v) thiourea were used for the desorption of the Hg-adsorbed MGO-SH adsorbent. Before this acid treatment, the magnetically recovered nanoadsorbent was washed first three times with deionized water to remove Hg (II) which was loosely attached to the vial or to the adsorbent itself. A 5 mL aliquot of the desorbent was then added and shaken for 30 min. The nanoadsorbent was separated magnetically from the desorbent, and its mercury concentration was determined. The experimental results indicated that 92% of the total adsorbed Hg (II) can be removed by 5.0 mL of 2.5 mol L^{-1} HCl and 2% (m/v) thiourea.

After the first regeneration, the adsorption studies were repeated. The nanoadsorbent was again regenerated and subjected to further use. The desorption efficiencies of the nanoadsorbent of the five reuses showed up to 4 cycles, there is no change in the Hg (II) sorption capacity of the MGO-HS. It could be concluded that the chemical bonding between mercapto group and magnetite plays a major role in retaining the capacity of the MGO-SH nanosorbents.

Fig. 10 Effect of co-existing cations on mercury removal
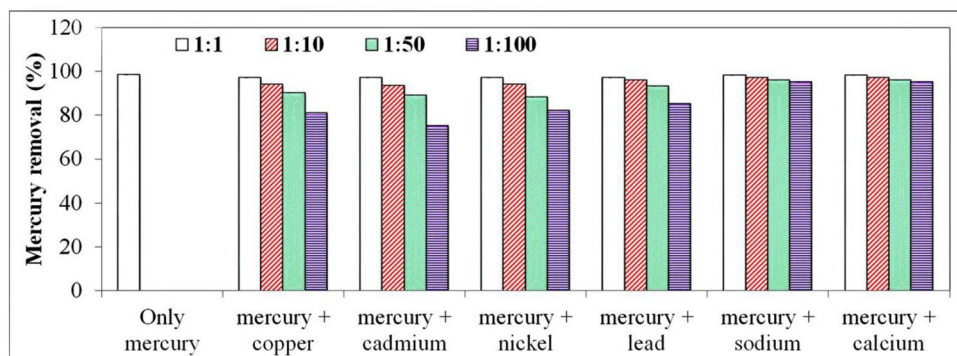
Table 4 Comparison of the proposed method with other reported methods for removal of Hg^{2+}

Adsorbent type	pH	Contact time	Adsorption capacity ($mg\,g^{-1}$)	References
$SH-Fe_3O_4$-MNPs	3	60 min	522.9	[46]
Mesoporous silica grafted with 1-furoyl thiourea	6	4 h	122.0	[58]
$Fe_3O_4@SiO_2$-SH	6.5	4 h	148.8	[59]
silica-coated $CoFe_2O_4$	5.5	60 min	19.8	[60]
Fe_3O_4/Au	7	60 min	79.59	[61]
Fe_3O_4-Ag^0	–	10 min	71.3	[1]
Zeolite-magnetite composites	–	24 h	22.1	[62]
CFA-derived Ag^0-nanocomposite	2	–	20.5–22.3	[63]
$CoFe_2O_4@SiO_2$-EDTA	7	6 h	103.3	[6]
Imino-diacetic acid IGO (Imino-IGO)	5	60 min	230	[47]
AAC cryogel	3.7	24 h	742	[64]
MGO-SH	6	20 min	550	This work

Comparison to other methods

To make a comparative perspective of the obtained results, some of the main parameters of the proposed method are compared with other methods used to remove mercury. Comparison of the results of the synthesized sorbent with the reported values of the similar studies (Table 4) showed that the proposed adsorbent has offered the highest maximum adsorption capacity. In addition, shorter adsorption time is another advantage of the proposed method over others.

Conclusions

Herein we have combined the extraction ability of mercapto grafted graphene with the advantages of magnetic nanoparticles to fabricate a new magnetic nanoadsorbent with a good tendency towards mercury ions. Some parameters such as contact time, adsorbent dosage, and pH were optimized and under optimal conditions, 98.5% of the Hg (II) was removed. The adsorption data followed the Freundlich

isotherm equation, and the adsorption was both endothermic and spontaneous. Although the synthesis of this sorbent is not economical yet, it offers some exciting advantages over the traditional methods and more studies are needed to make it more affordable. Ease of separation by an external magnetic field, simple recovery, its reuse and regeneration are some of these advantages.

Author contributions Maryam Karimi: Conceptualization, Investigation, Validation, Writing—review & editing. Mostafa Hassanisadi: Investigation, Project administration, Writing—review & editing. Tahereh Poursaberi: Conceptualization, Supervision, Writing—review & editing.

Declarations

Conflict of interest No potential conflict of interest was reported by the authors.

Ethical approval This article does not contain any studies with human participants or animals performed by any of the authors.

Informed consent Informed consent was obtained from all individual participants included in the study.

References

1. V.J. Inglezakis, A. Kurbanova, A. Molkenova, A.A. Zorpas, TSh. Atabaev, Sustainability **12**, 5489–5498 (2020)
2. Y. Vicente-Martinez, M. Caravaca, A. Soto-Meca, Environ. Chem. Lett. **18**, 975–981 (2020)
3. M.I. Litter, Appl. Catal. B **23**, 89–114 (1999)
4. L.D. Lau, R. Rodriguez, S. Hennery, D. Manuel, Environ. Sci. Technol. **32**, 670–675 (1998)
5. S.G. Bottta, D.J. Rodriguez, A.G. Leyva, M.I. Litter, Catal. Today **76**, 247–258 (2002)
6. K. Xia, Y. Guo, Q. Shao, Q. Zan, R. Bai, Nanomaterials **9**, 1532–1554 (2019)
7. S.E. Bone, J.R. Bargar, G. Sposito, Environ. Sci. Technol. **48**, 10681–10689 (2014)
8. S. Chiarle, M. Ratto, M. Rovatti, Water Res. **34**, 2971–2978 (2000)
9. S. Jana, M.K. Purkait, K. Mohanty, Desalin. Water Treat. **37**, 321–330 (2012)
10. O. Hakami, Y. Zhang, C.J. Banks, Water Res. **46**, 3913–3922 (2012)
11. L. Wang, D. Hou, Y. Cao, Y.S. Ok, F.M.G. Tack, J. Rinklebe, D. O'Connor, Environ. Int. **134**, 105281 (2020)
12. H. Liu, W. Ruan, Z. Zhang, Y. Zhou, F. Shen, J. Liu, H. Yang, Fuel **309**, 122238 (2022)
13. M. Zhou, X. Xie, Q. Liu, M. Zhang, C. Peng, F. Li, Q. Liu, Y. Song, J. Wu, Z. Qiao, Chem. Eng. J. **430**, 132857 (2022)
14. T. Tene, S. Bellucci, M. Guevara, E. Viteri, M.A. Polanco, O. Salguero, E. Vera-Guzmán, S. Valladares, A. Scarcello, F. Alessandro, L.S. Caputi, C.V. Gomez, Nanomaterials **12**, 309 (2022)
15. E. Hosseinpournajjar, A.H. Kianfar, M. Dinari, J. Iran. Chem. Soc. (2022). https://doi.org/10.1007/s13738-021-02437-z
16. Y. Zhang, Y. Zhang, R. Qu, X. Geng, X. Kong, C. Sun, C. Ji, Y. Wang, Sep. Purif. Technol. **282**, 120147 (2022)
17. S. Li, H. Xu, L. Wang, L. Ji, X. Li, Z. Qu, N. Yan, J. Hazard. Mater. **403**, 123940 (2021)
18. T. Mustafa, A. Sarı, M.R. Afshar Mogaddam, S. Kaya, K.P. Katin, N. Altunay, Mater. Chem. Phys. **277**, 125501 (2022)
19. X. Lu, J. Jiang, K. Sun, J. Wang, Y. Zhang, Mar. Pollut. Bull. **78**, 69–76 (2014)
20. Z.V.P. Murthy, P.A. Parikh, N.B. Patel, J. Dispers. Sci. Technol. **34**, 747–755 (2013)
21. J.-G. Yu, B.-Y. Yue, X.-W. Wu, Q. Liu, F.-P. Jiao, X.-Y. Jiang, X.-Q. Chen, Environ. Sci. Pollut. Res. **23**, 5056–5076 (2016)
22. H. Zhu, Y. Shen, Q. Wang, K. Chen, X. Wang, G. Zhang, J. Yang, Y. Guo, R. Bai, RSC Adv. **7**, 39204–39215 (2017)
23. J. Yan, T. Wei, W. Qiao, B. Shao, Q. Zhao, L. Zhang, Z. Fan, Electrochim. Acta **55**, 6973–6978 (2010)
24. Y. Zhu, S. Murali, W. Cai, X. Li, J.W. Suk, J.R. Potts, R.S. Ruoff, Adv. Mater. **22**, 3906–3924 (2010)
25. K. Molaei, H. Bagheri, A.A. Asgharinezhad, H. Ebrahimzadeh, M. Shamsipur, Talanta **167**, 607–616 (2017)
26. Z. Zhang, H. Li, H. Sui, L. He, X. Li, RSC Adv. **8**, 15813–15824 (2018)
27. H. Bagheri, A. Afkhami, M. Saber-Tehrani, H. Khoshsafar, Talanta **97**, 87–95 (2012)
28. M. Castro, J. Cruz, E. Otazo-Sánchez, L. Perez-Marín, J. Phys. Chem. A **107**, 9000–9007 (2003)
29. L. Perez-Marín, M. Castro, E. Otazo-Sánchez, G.A. Cisneros, Int. J. Quantum Chem. **80**, 609–622 (2000)
30. J.K. Sahoo, S.K. Paikra, A. Baliarsingh, D. Panda, S. Rath, M. Mishra, H. Sahoo, Nano Express **1** (2020)
31. E. Erdem, G. Çölgeçen, R. Donat, J. Colloid Interface Sci. **282**, 314–319 (2005)
32. I.A.W. Tan, A.L. Ahmad, B.H. Hameed, J. Hazard. Mater. **154**, 337–346 (2008)
33. I. Langmuir, J. Am. Chem. Soc. **40**, 1361–1403 (1918)
34. O. Redlich, D.L. Peterson, J. Phys. Chem. **63**, 1024–1026 (1959)
35. T.P. O'Connor, J. Muller, Micropor. Mesopor. Mater. **46**, 341–349 (2001)
36. J.H. Chun, S.K. Jeon, N.Y. Kim, J.Y. Chun, Int. J. Hydrog. Energy **30**, 1423–1436 (2005)
37. K. Zhang, L.L. Zhang, X.S. Zhao, J. Wu, Chem. Mater. **22**, 1392–1401 (2010)
38. X.-Z. Tang, W. Li, Z.-Z. Yu, M.A. Rafiee, J. Rafiee, F. Yavari, N. Koratkar, Carbon **49**, 1258–1265 (2011)
39. E. Fourest, B. Volesky, Environ. Sci. Technol. **30**, 277–282 (1996)
40. J. Gardea-Torresdey, M. Hejazi, K. Tiemann, J.G. Parsons, M. Duarte-Gardea, J. Henning, J. Hazard. Mater. **91**, 95–112 (2002)
41. R.G. Pearson, J. Am. Chem. Soc. **85**, 3533–3539 (1963)
42. C. Jeon, W.H. Höll, Water Res. **37**, 4770–4780 (2003)
43. A. Denizli, S. Bektaş, Y. Arıca, Ö. Genç, J. Appl. Polym. Sci. **97**, 1213–1219 (2005)
44. G. Hilson, Sci. Total Environ. **362**, 1–14 (2006)
45. S.K. Srivastava, R. Tyagi, N. Pant, Water Res. **23**, 1161–1165 (1989)
46. S. Pan, H. Shen, Q. Xu, J. Luo, M. Hu, J. Colloid Interface Sci. **365**, 204–212 (2012)
47. F.S. Awad, K.M. AbouZied, W.M. Abou El-Maaty, A.M. El-Wakil, M.S. El-Shall, Arab. J. Chem. **13**, 2659–2670 (2020)
48. J. De Clercq, Int. J. Ind. Chem. **3**, 1 (2012)
49. Y. Seki, K. Yurdakoc, Adsorption **12**, 89–100 (2006)
50. Y. Yu, Y.Y. Zhuang, Z.H. Wang, J. Colloid Interface Sci. **242**, 288–293 (2001)
51. N.N. Nassar, J. Hazard. Mater. **184**, 538–546 (2010)
52. S.P. Mishra, D. Tiwari, R.S. Dubey, M. Mishra, Bioresour. Technol. **63**, 1–5 (1998)
53. X. Luo, L. Zhang, J. Hazard. Mater. **171**, 340–347 (2009)
54. F.S. Zhang, H. Itoh, J. Hazard. Mater. **101**, 323–337 (2003)
55. M. Hirata, N. Kawasaki, T. Nakamura, K. Matsumoto, M. Kabayama, T. Tamura, S. Tanada, J. Colloid Interface Sci. **254**, 17–22 (2002)
56. X. Pu, Z. Jiang, B. Hu, H. Wang, J. Anal. At. Spectrom. **19**, 984–989 (2004)
57. C. Huang, B. Hu, Spectrochim. Acta Part B At. Spectrosc. **63**, 437–444 (2008)
58. M. Mureseanu, A. Reiss, N. Cioatera, I. Trandafir, V. Hulea, J. Hazard. Mater. **182**, 197–203 (2010)
59. S. Zhang, Y. Zhang, J. Liu, Q. Xu, H. Xiao, X. Wang, H. Xu, J. Zhou, Chem. Eng. J. **226**, 30–38 (2013)
60. B.Y. Song, Y. Eom, T.G. Lee, Appl. Surf. Sci. **257**, 4754–4759 (2011)
61. L.F.O. Maia, M.S. Santos, T.G. Andrade, R.C. Hott, M.C.S. Faria, L.C.A. Oliveira, M.C. Pereira, J.L. Rodrigues, Environ. Technol. **41**, 959–970 (2020)
62. A.L. Andrade, L.C.D. Cavalcante, J.D. Fabris, M.C. Pereira, J.D. Ardisson, C. Pizarro, Hyperfine Interact. **240**, 18–23 (2019)
63. Z. Tauanov, J. Lee, V.J. Inglezakis, J. Mol. Liq. **305**, 112825 (2020)
64. A.Z. Baimenov, D.A. Berillo, K. Moustakas, V.J. Inglezakis, J. Hazard. Mater. **399**, 123056 (2020)